TRAINABLE WEKA SEGMENTATION: MACHINE LEARNING AND AI TOOL FOR QUANTIFICATION OF HYBRID SINTERED SILVER MICROSTRUCTURAL EVOLUTION

Marty Lorgino D. Pulutan
Kimberly P. Jardin
Renald L. Dechino

Backend Technologies
Ampleon Philippines, Inc., Light Industry & Science Park I, Brgy. Diezmo, Cabuyao City, Laguna
marty.lorgino.pulutan@ampleon.com

ABSTRACT

The thermal reliability of GaN-based power devices is heavily influenced by the structural integrity of the die attach layer, particularly under prolonged high-temperature storage (HTS) conditions. The study investigates the microstructural evolution of hybrid sintered silver Ag die attach material and its impact on thermal resistivity (R_{th}) through machine learning and AI-based image analysis. Scanning Electron Microscopy (SEM) cross-sections were processed using Trainable Weka Segmentation (TWS), a machine learning tool for pixel-level classification. Fractal descriptors – lacunarity (λ) and succolarity (S_u)—were computed to quantify spatial heterogeneity and network connectivity of the sintered Ag microstructure obtained from macro program based on TWS and computational framework. Results revealed that thermal ageing leads to increased λ and decreased S_u, indicative of grain coarsening and reduced interconnectivity. Such changes were strongly correlated with shifts in R_{th}, with regression models yielding R^2 values of 0.892 (λ), 0.961 (S_u), and 0.938 (combined). The study presents a novel AI-assisted image analysis framework designed to investigate and characterize microstructural evolution using fractal parameters as numerical descriptors, providing a quantitative basis for assessing the thermal reliability of sintered silver die attach materials.

1. 0 INTRODUCTION

The long-term reliability of GaN-based power devices is primarily governed by the structural and thermal stability of the die attach interface, with die attach degradation emerging as a dominant failure mechanism under prolonged thermal ageing. Elevated temperatures induce a significant increase in thermal boundary resistance (TBR) at the die attach interface thereby impeding effective heat dissipation and diminishing overall thermal management efficiency. Such degradation has been closely associated with the microstructural evolution of the Ag sinter which is a commonly utilized die attach material in RF power industry. Findings from HTS tests conducted at 200 °C have consistently demonstrated a progressive rise in TBR over time based on previous evaluation conducted. Microstructural analysis via cross-sectional imaging of aged samples revealed notable morphological transformations within the Ag sinter layer, including pore coalescence, grain growth, and structural disintegration—all of which contribute to increased thermal resistance and premature failure of the thermal pathway.

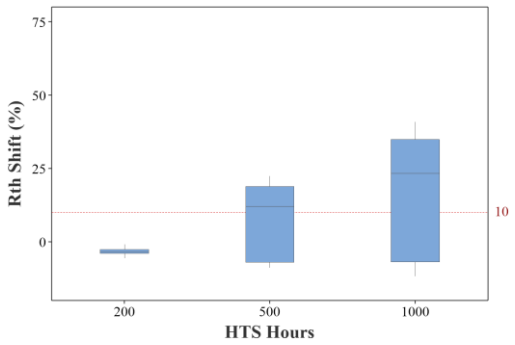

Fig. 1. Percent Shift in Thermal Resistance (R_{th}) of the ACC After 200, 500, and 1000 Hours of High Temperature Storage (HTS).

The kinetics of such microstructural transformations are highly temperature-dependent. At elevated ageing temperatures, diffusion of Ag particles triggers grain coarsening, void formation, and the expansion of resin-rich zones, deteriorating the sintered network's thermal conductivity. Conversely, lower ageing temperatures result in a slower densification and limited coarsening, thereby moderating the rate of TBR escalation. The thermally activated behavior points to a critical need for investigating the fundamental mechanisms governing sintered Ag degradation and their implications on device-level R_{th}.

Despite the increasing adoption of hybrid Ag sinter materials in RF and high-power electronic applications, there is no existing comprehensive study or literature that quantitatively correlates microstructural evolution with thermal resistivity (R_{th}). To address the gap, the present work utilizes advanced post-processed image analysis and artificial intelligence (AI)-assisted segmentation techniques to extract fractal-based

descriptors—such as lacunarity (λ) and succolarity (S_u)—from scanning electron microscopy (SEM) images. These fractal parameters serve as quantitative indicators of microstructural complexity, including pore topology, grain boundary integrity, and sintered network interconnectivity. By establishing a correlation between these descriptors and measured R_{th}, this study introduces a novel framework for characterizing time- and temperature-dependent degradation of Ag sinter via fractal analysis—thus offering new insights into predictive thermal reliability modeling of GaN power devices.

2. 0 REVIEW OF RELATED WORK

One of the machine learning-based image tool analysis used to quantify microstructural changes in materials is the Trainable Weka Segmentation (TWS) - a plugin for the Fiji platform that facilitates supervised pixel classification using machine learning algorithms. Arganda-Carreras et al.[1] introduced TWS as a highly flexible, user-friendly solution capable of handling diverse microscopy data including light, fluorescence, and electron microscopy images. By enabling users to train classifiers on representative features, the tool improves the accuracy and reproducibility of segmentation that is critical for analyzing structural heterogeneity in complex materials. Baranov et al.[2] applied TWS to transmission electron microscopy (TEM) images of inorganic nanoparticles. The study underscored the challenges of traditional segmentation approaches in handling low contrast and high background noise typical in high-resolution TEM imaging. Through classifier training tailored to particle morphology, the researchers achieved consistent segmentation of nanoparticles which enabled precise quantification of particle size distributions and morphologies, highlighting TWS's capacity to be adapted to domain-specific imaging challenges in nanostructured materials.

The TWS is relevant to the investigation of microstructural evolution in sintered silver during thermal ageing where accurate segmentation is critical to monitor grain growth, pore structure, and interconnectivity over time. Thermal ageing induces significant changes in sintered silver's microstructure including coarsening of grains, densification, and changes in porosity—all of which should be analyzed using high-resolution microscopy combined with reliable image segmentation. Manual segmentation of such features is often impractical and prone to inconsistency, especially across large datasets or time series studies. The pixel-based machine learning approach offered by TWS allows for consistent and automated tracking of these microstructural parameters across different agein×g durations and temperatures.

Several studies have substantiated the observed structural transformations of sintered Ag during thermal ageing. Chen et al.[3] reported that thermal ageing at 250°C promotes the formation of necks between adjacent Ag flakes due to nanoparticle coarsening thereby enhancing adhesion on ENEPIG substrates. The behavior was attributed to the Ostwald Ripening mechanism where pores increase in size while decreasing in number with extended exposure. Additionally, interdiffusion of Au and Ag during thermal ageing was observed to form thermally stable Ag-Au solid solutions further supported by increased Au grain size. In a related investigation, Chen et al.[4] quantitatively analyzed the microstructural evolution of Ag sinter paste under high-temperature ageing in both air and vacuum conditions. The study revealed a pronounced coarsening effect in oxygen-rich environments where Ag oxidized to form AgO_2, leading to the formation of Ag nanoparticles that clustered within the sintered matrix. Moreover, diffusion of Ag from the metallization layer into the sintered bulk was found to reduce interfacial stress and promote grain and pore growth at elevated temperatures.

Such findings emphasize the critical role of automated segmentation tools like TWS in accurately capturing and quantifying thermally driven microstructural changes in sintered materials. By bridging high-resolution imaging and machine learning, TWS provides a scalable solution for monitoring the evolution of material systems subjected to complex ageing environments.

3.0 METHODOLOGY

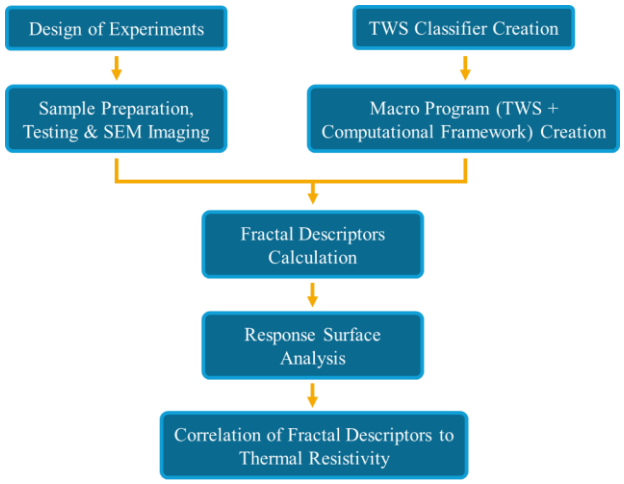

Fig. 1. Schematic Diagram of the Methodological Workflow Implemented in the Study.

3.1 Experimental Design and Sample Preparation

A full-factorial Design of Experiments (DoE) was implemented using a 3-factor model to investigate the effects of package type, package dimensions and HTS temperature (refer to Table 1 for the factor levels) on microstructural

evolution and R_{th} performance. The experimental matrix consisted of 12 legs each representing a unique combination of the aforementioned factors. For each leg, 30 units of the designated package configuration were assembled and subjected to electrical testing to extract R_{th} parameter. From each leg, two representative units were selected for microstructural analysis. Cross-sectional preparation targeted the central region of the die to capture critical die attach behavior. The prepared samples were subsequently imaged using a floor-type Scanning Electron Microscope (SEM) and the generated micrographs were later processed using advanced image analysis techniques for fractal quantification.

3.2 Trainable Weka Segmentation and Macro Program Creation

The Fiji image processing software was installed on the workstation connected to the floor-type SEM to facilitate direct integration of image acquisition and microstructural quantification workflows. A classifier recipe was developed using a representative cross-sectional image randomly selected from the pool of SEM micrographs acquired across different experimental legs through TWS. To streamline processing, a macro program was created by embedding a sequence of commands within the Fiji environment. The macro program invoked the TWS module for segmentation which uses Gaussian Blur, Laplacian, Sobel, Gabor Filter and Anisotropic Diffusion, and then sequentially executed the computation of fractal descriptors and was compiled and deployed as a Fiji plug-in, allowing seamless batch processing. Upon execution, the plug-in autonomously retrieved SEM images from the designated folder, performed segmentation of region of interest (ROI) whether the sintered particles or resin/void, computed fractal metrics, and generated both graphical plots and raw numerical outputs. Classified images with segmentation overlays were also produced as part of the output, enabling visual validation of phase recognition and quantitative analysis.

3.3 Data Analysis and Modeling

Response Surface Analysis (RSA) was performed using Minitab version 20.4 to identify statistically significant factors influencing λ, S_u, and R_{th}. For visualization and trend analysis, λ and S_u values obtained from each experimental leg were plotted using Matplotlib in Python, allowing comparison across varying HTS temperatures within each package type configuration. To explore the relationship between microstructural descriptors and thermal performance, R_{th} values corresponding to each measured λ and S_u value were plotted and analyzed using linear regression techniques. Regression models were developed independently for λ and S_u and subsequently integrated using multiple linear regression to formulate a predictive equation expressing R_{th} as a function of both descriptors.

4.0 RESULTS AND DISCUSSION

4.1 Trainable Weka Segmentation for Sintered Ag Distinction

The analysis of the Scanning Electron Microscopy (SEM) micrographs was conducted using the TWS plugin integrated within the Fiji distribution of ImageJ – a machine learning-based tool enabling pixel-level classification through supervised learning. For each experimental sample, the acquired SEM images were loaded directly into the TWS interface installed on the SEM workstation which then facilitated the segmentation and extraction of microstructural features, as illustrated in the subsequent figure.

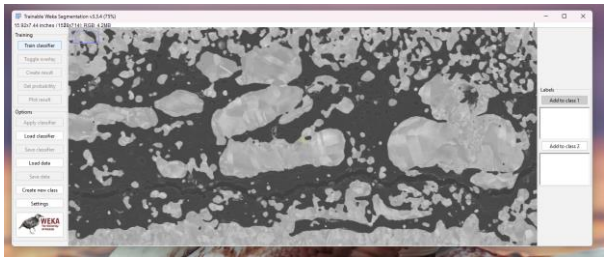

Fig. 2. Graphic User Interface of TWS with the Loaded SEM Image.

The TWS algorithm was trained to differentiate sintered Ag particles from the resin matrix and void regions. Manual annotations were performed using the freehand selection tool wherein representative regions were precisely outlined to correspond exclusively to either Ag particles or resin/void. During the annotation procedure, spatial discrimination protocols were implemented to ensure that resin regions were not inadvertently enclosed within the segmentation boundaries designated for Ag particles and vice versa.

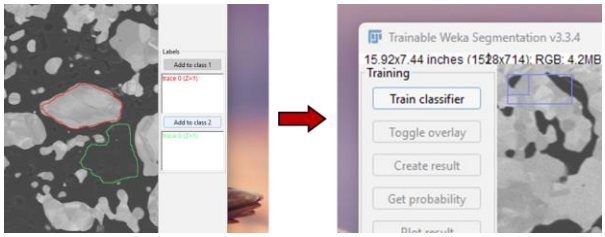

Fig. 3. Segmentation and Classifier Training Process Using TWS. Sintered Ag particles are annotated in red while the rest of resin and voids are outlined in green for sample classification.

Following the annotation and classification of multiple representative regions corresponding to the ROI within the SEM micrographs, the TWS algorithm was trained to perform automated pixel-based classification. Upon successful training, Ag particles were visually mapped in red

while the resin and void regions were rendered in green for segmentation validation.

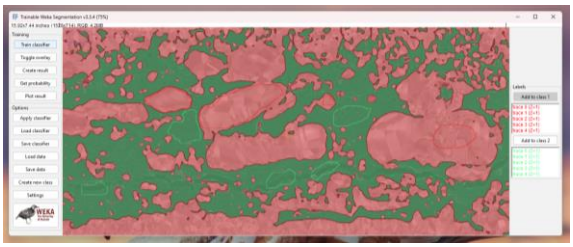

Fig. 4. Segmentation Output of Sintered Ag Against Resin and Void. The image shows classified regions where Class 1 (voids and pores) is highlighted in green and Class 2 (solid Ag matrix) in red demonstrating effective pixel classification based on the trained model.

The resulting classified output was juxtaposed with the original SEM image to assess the accuracy of phase recognition and to verify that no boundary overlaps occurred between the distinct material phases. A dedicated classifier protocol or 'recipe' was developed specifically for cross-sectional images of Ag sinter joints ensuring consistent and reproducible segmentation across all analyzed samples.

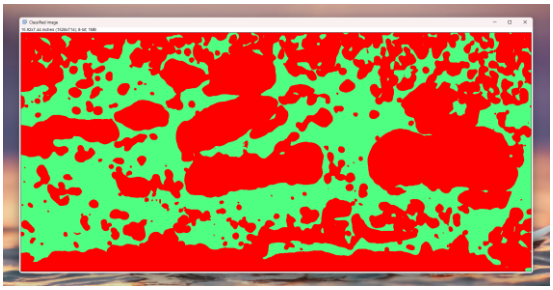

Fig. 5. Final Classified Output Image from TWS Showing Binary Segmentation Results. The segmented regions represent pores and voids (green) and solid Ag matrix (red) used as input for further fractal analysis and quantification of microstructural features.

To evaluate the flexibility of the developed segmentation recipe, five additional SEM images with different magnifications, spatial location along the sintered bond line, and microstructural appearance (see Fig. 12 in Appendix) were analyzed. The pre-trained classifier was applied, enabling automated segmentation across diverse conditions. All image samples were segmented and classified with high visual and spatial accuracy, independent of variations in particle morphology, and grayscale intensity. Consistent performance across heterogeneous imaging scenarios confirms the applicability of the classifier for comprehensive microstructural analysis of sintered Ag interfaces.

4.2 Macro Program for Calculation of Fractal Descriptors Using TWS and Computational Framework Plug-in

A macro-driven computational framework was developed to facilitate automated fractal analysis of microstructural features of the cross-sectional image of sintered Ag at time-zero and after HTS read points. The custom program integrates the machine learning and AI capabilities of the TWS algorithm with an open-source platform engineered for analyzing complex and non-linear systems. The macro was programmed to autonomously retrieve each image from the dedicated directory, apply the pre-trained TWS classifier for pixel-level segmentation, and compute for fractal descriptors.

The λ was calculated using Equation 1 to assess the degree of spatial inhomogeneity, capturing the distribution of resin and voids within the segmented sintered structure using sliding-box algorithm for the scanning method. A high λ value indicates a more heterogeneous arrangement of Ag particles while lower values correspond to uniform particle dispersion. A second fractal descriptor which is the S_u was computed to evaluate the relative ease of percolation within the conductive matrix, reflecting the geometric complexity and connectivity of sintered Ag networks, and is calculated using Equation 2 using the same scanning method.

The computational framework integrated with TWS for lacunarity and succolarity analysis was configured using a seven-tier box size range spanning from 1×1 to 64×64 pixels based from the scale of the SEM images used in the study. The sliding box algorithm was adopted as the scanning method for characterizing highly complex structures and fine particulate features. For succolarity analysis, the flooding direction was set to T2D (Top-to-Down) representing the percolative behavior of thermal conduction from the die's active surface toward the heatsink interface.

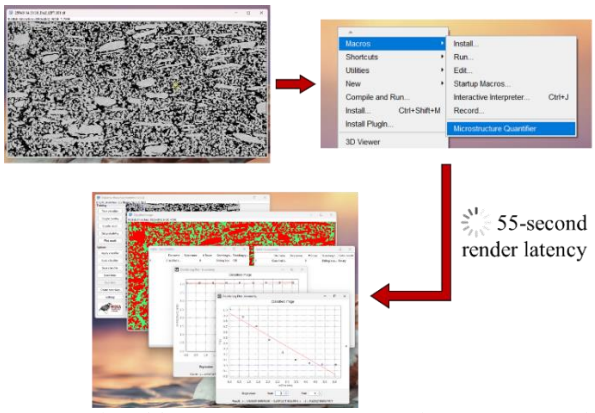

Fig. 6. Execution of the Custom Macro Program "Microstructure Quantifier" Within the Fiji Environment.

$$\lambda(r) = \frac{E[(M^2(r)]}{E^2[(M(r)]} \quad (Equation\ 1)^5$$

$$\sigma(BS(k), dir) = \frac{\sum_{k=1}^{n} OP(BS(k)) \times PR(BS(k), pc)}{\sum_{k=1}^{n} PR(BS(k), pc)} \quad (Equation\ 2)^6$$

Each complete execution of the macro including image loading, segmentation, descriptor computation, and graphical rendering was accomplished within approximately 55

seconds per image. Outputs include numerical values for λ and S_u normalized to the image area in pixels along with visualization plots displaying segmentation overlays and structural descriptors. The resulting data enables systematic and reproducible quantification of microstructural complexity across varying sample conditions, supporting comprehensive morphometric analysis as quantitative differentiator of microstructural evolution of every HTS condition and readpoint.

4.3 Application of the Machine Learning and AI-Based Macro Program on Thermal Resistivity Shift after HTS

In order to identify the underlying factors contributing to the observed R_{th} shift exceeding 10% in the ACC package employing a hybrid Ag sinter die attach material after 500 hours of HTS at 200 °C, a Full Factorial Design of Experiments (DoE) was implemented. The experimental matrix was structured to systematically evaluate the influence of multiple variables on the microstructural evolution of the sintered joint after 500 hours of thermal aging as shown on Table 1.

Table 1. DOE Parameters: Factors and Associated Levels

Variables	Code	Levels
HTS Temperature	A	150 ºC, 175 ºC, 200ºC
Package Type	B	ACC, OMP
Package Dimension	C	800 (20×10×5 mm), 1250 (32×10×5 mm)

For each experimental leg, the recorded response variables included λ and S_u values extracted from the macro-based fractal analysis along with the corresponding average R_{th} and percentage shift after aging. A Response Surface Analysis (RSA) was employed to model the relationships between the microstructural descriptors and process parameters.

Table 2. RSA Results for Lacunarity and Succolarity

Factor Code	Lacunarity		Succolarity	
	% Impact	P-Value	% Impact	P-Value
A	31.87	0.000	19.24	0.000
B	52.84	0.000	68.46	0.000
A^2	3.09	0.021	4.02	0.009
A · B	9.75	0.001	6.02	0.000

Following the elimination of statistically insignificant factors and interaction terms, the adjusted coefficients of determination (R^2_{adj}) for λ and S_u were found to be 96.14% and 99.58% respectively. Such values indicate a strong predictive capability of the refined models suggesting that the selected input variables are highly effective in capturing the variance in microstructural evolution across different test conditions.

Based on the results, package type and HTS temperature are both significant factors while package dimension does influence the microstructural evolution of sintered Ag structure based on both λ and S_u (calculated using Adj. SS).

Detailed examination of cross-sectional SEM micrographs comparing the ACC and OMP configurations under identical HTS conditions (500 hours at 200 °C), as shown in Fig. 7, revealed pronounced microstructural disparities. In the ACC configuration, a greater percentage of the cross-sectional area was occupied by resin, and sintered Ag particles exhibited a more compact and clustered morphology in relative comparison to the distribution observed in the OMP counterpart. Additional morphological features observed in the ACC samples included migration of Ag particles toward the backside metallization (BSM) and Au-plated die pad as well as noticeably coarsened grain structures. The presence of such features is indicative of accelerated microstructural evolution potentially driven by environmental differences inherent to the package architecture. The findings corroborate the assertion made by Chen et al., wherein the distinct microstructural characteristics observed under varying HTS temperatures are primarily attributed to the presence of ambient air in ACC and the vacuum-like environment characteristic of OMP. Such environmental conditions influence the diffusion kinetics and oxidation behavior during thermal aging thereby contributing to the divergence in microstructural evolution across package types[3].

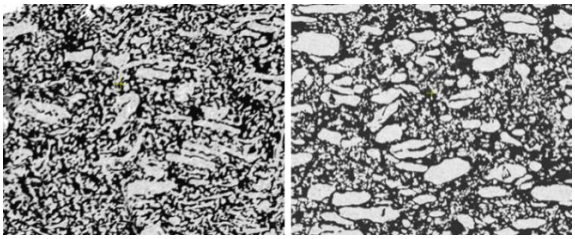

Fig. 7. Cross-Sectional SEM Images of OMP (left) and ACC (right) at 2500× Magnification Subjected to 500 Hours of HTS at 200ºC .

Extending the HTS duration to 1000 hours at 200 °C resulted in pronounced grain coarsening and a substantial increase in the resin-occupied area fraction. The expansion of resin-rich regions contributed to a noticeable reduction in the interconnectivity of the sintered silver grain network. Fig. 7 illustrates cross-sectional micrographs of the ACC configuration from time-zero to 1000 hours of aging. The microstructure progressively evolved toward a less dense and more disconnected conductive network. Such morphological changes are indicative of advanced degradation, potentially compromising thermal and electrical performance due to

diminished percolation pathways. Although visual assessment strongly suggests advanced microstructural transformation in the ACC samples, the comparison remains largely qualitative and subjective. A more definitive evaluation requires the application of quantifiable metrics capable of capturing changes in structural organization as a function of process variables. Fractal descriptors such as λ and S_u provide a mathematically rigorous means of quantifying microstructural evolution and enable objective differentiation of material responses influenced by package type, HTS duration, and thermal exposure conditions.

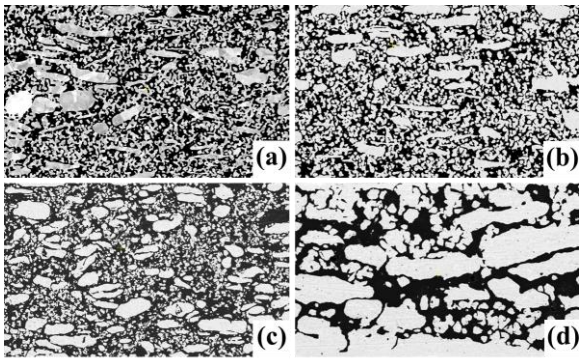

Fig. 8. Cross-Sectional SEM Images of ACC at (a) time-zero, (b) 200 hours, (c) 500 hours and (d) 1000 hours at 2500× magnification of HTS at 200°C.

Experimental legs subjected to identical package types and HTS temperatures regardless of package dimensions exhibited comparable fractal descriptor values thereby reinforcing the earlier statistical conclusion regarding the insignificance of geometric size. The λ exhibited a consistent upward trend while S_u decreased progressively when plotted against HTS temperature. Such opposing trends suggest that elevated temperatures promote increased microstructural disorder and reduced interconnectivity among sintered Ag particles indicating thermally driven evolution.

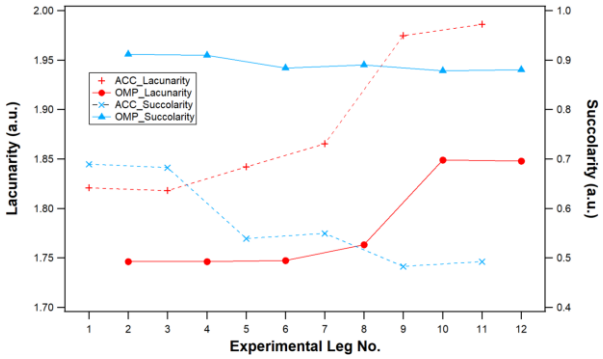

Fig. 9. Experimental Leg-Wise Variation in Lacunarity (top) and Succolarity (bottom) for ACC and OMP Packages.

In Fig. 9, λ values remained relatively constant within the 150 °C to 175 °C range but exhibited a pronounced increase at 200 °C. The sharp rise implies the activation of Ostwald Ripening at elevated temperatures, a phenomenon characterized by coarsening and growth of sintered Ag particles and resin domains leading to fewer but larger features and increased spatial heterogeneity[4]. Notably, λ values for the OMP configuration at 200 °C approached those of the ACC package at 175 °C, whereas the ACC package subjected to 200 °C demonstrated substantially higher λ, correlating with observed R_{th} shifts exceeding the 10% performance threshold (see Fig. 13 in Appendix).

The S_u trends further elucidate the thermal degradation behavior. While the OMP configuration exhibited only a marginal reduction in S_u with increasing HTS temperature, the ACC configuration showed a marked and nonlinear decline. Such behavior suggests significant disruption in particle connectivity, resulting in reduced percolation pathways for thermal conduction. The severe drop in S_u for ACC samples aligns with the concurrent rise in λ, collectively indicating that sintered Ag structures are undergoing rapid coarsening and disconnection at elevated thermal exposure, consistent with Ostwald Ripening mechanisms.

Such observations point to potential thermal aging limitations inherent to each package architecture. Specifically, the ACC configuration appears more susceptible to microstructural instability beyond 175 °C where accelerated particle coarsening compromises both structural continuity and thermal performance. Sintered Ag materials may thus require stabilization within a defined phase regime to avoid exceeding critical resistivity thresholds and prevent functional failure in high-temperature applications.

To further validate the observations, λ and S_u values were statistically correlated with the corresponding average R_{th} measurements. The objective was to determine the degree of association between microstructural descriptors and functional performance metrics and to derive predictive relationships that could inform process and reliability guidelines for sintered die attach materials.

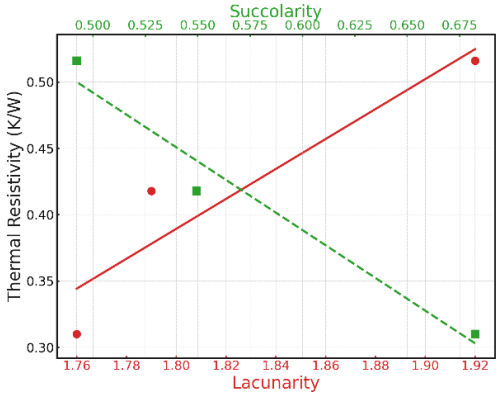

Fig. 10. Correlation Plots of Thermal Resistivity Against Lacunarity (red) and Succolarity (green) of ACC Package.

A strong correlation was established between the computed fractal descriptors λ and S_u and the measured R_{th} as indicated by coefficients of determination of 0.892 and 0.961, respectively. Such high values reflect a strong predictive relationship suggesting that microstructural features quantified via fractal analysis can serve as reliable indicators of R_{th} performance. The predictive power of the descriptors implies that the degree of microstructural disorder and connectivity as captured by λ and S_u, can be used to anticipate whether R_{th} will exceed critical design thresholds.

Linear regression yielded the following predictive equations:

From λ,

$$R_{th} = 1.128\lambda - 1.641$$

From S_u,

$$R_{th} = -1.036S_u + 1.010$$

Incorporating both descriptors into a multiple linear regression model produced an enhanced expression:

$$R_{th} = 0.441\lambda - 0.713S_u + 0.021$$

The combined model achieved a coefficient of determination of 0.938, indicating excellent predictive accuracy when both spatial heterogeneity and connectivity metrics are used as input variables. The model was further analyzed to define structural specifications. Based on the regression analysis, R_{th} shifts remain within acceptable limits (less than 10%) when λ does not exceed 1.87 and S_u remains above 0.50. Such thresholds provide a quantifiable basis for interpreting cross-sectional micrographs and assessing the potential risk of thermal performance degradation.

The analysis enabled the establishment of a quantitative framework for describing and comparing microstructures post-HTS. Furthermore, the findings offer scientific and mathematical validation that microstructural evolution plays a critical role in R_{th} shifts, thereby identifying a potential root cause for performance failure in accelerated thermal stress testing.

5.0 CONCLUSION

The study establishes a quantitative approach in describing the microstructural evolution of hybrid sintered Ag during thermal ageing as an effective approach in failure analysis of the out-of-specification shifts of R_{th}. The observed increase in thermal boundary resistance is closely associated with temperature-driven morphological changes in the Ag sinter including grain coarsening, pore growth, and disruption of interfacial connectivity. By applying advanced AI-based image segmentation and extracting fractal descriptors such as λ and S_u, the evolution of microstructural complexity was successfully correlated with R_{th} as inference of thermal limitation of hybrid sintered Ag on each package type. The findings not only validate the critical role of sintered structure in thermal performance but also demonstrate the potential of fractal analysis as a predictive tool for reliability assessment in high-temperature power applications.

6.0 RECOMMENDATIONS

To further improve the study, it is recommended that future studies incorporate HTS time readpoints at multiple intervals per temperature condition. The addition would enable calculation of the thermal acceleration constant and facilitate a more accurate modeling of microstructural degradation kinetics. Further validation of the methodology can also be pursued by applying the analysis to pure Ag sinter type thereby allowing comparison of microstructural evolution rates between hybrid and pure Ag die attach materials. In addition, expanding the scope of the study to include other RF power package types such as Quad Flat No-Lead (QFN) and Land Grid Array (LGA) configurations would support a more comprehensive understanding of the thermal performance limits of hybrid sintered Ag across diverse package architectures.

7.0 ACKNOWLEDGMENT

The authors extend their appreciation to the technicians of the Failure Analysis & Reliability Department, Back-end Technologies (BET), New Product Introduction (NPI), NPI/BET Quality Inspectors for their support in the execution of the experiments, and to Ampleon Philippines, Inc. management team for their support.

8.0 REFERENCES

1. I. Arganda-Carreras, et al., ***Bioinformatics***, *33(15)*, **2017**, 2424-2426.
2. C. G. Bell, et al., ***J. Microsc.***, *288(3)*, **2022**. 169-184.
3. C. Chen, et al., ***J. Alloys Compd.***, *834*, **2020**, 155173**.**
4. C. Chen, et al., ***J. Alloys Compd.***, *828*, **2020**, 154397**.**
5. K. Sengupta, K. J. Vinoy, ***Fractals***, *14(04)*, **2006**, 271-282**.**
6. R. H. C De Melo, A. Conci, ***IWSSIP 2008***, **2008**, 291-294**.**

9.0 ABOUT THE AUTHORS

Marty Lorgino D. Pulutan received the B. S. degree in Applied Physics specializing in Materials Physics from University of the Philippines, Los Baños in 2017 and currently pursuing M. S. degree in Materials Science and Engineering by Research in Mapua University. He has published a total of 10 papers in peer-reviewed journals and international conference proceedings. He is currently a Senior Materials Development Engineer under Back End Technologies Department in Ampleon Philippines, Inc.

Kimberly P. Jardin graduated from De La Salle University Manila with a bachelor's degree in chemical engineering. She also graduated from the Ateneo Graduate School of Business with a master's degree in business administration (MBA). She is currently working for Ampleon Philippines, Inc. as a Senior Quality Engineer in NPI/Back-end Technology Quality.

Renald L. Dechino joined Ampleon Netherlands BV in July 2023 as a Senior Failure Analysis Engineer. He graduated from the University of Saint La Salle, Bacolod City with a bachelor's degree in Materials Engineering.

10.0 APPENDIX

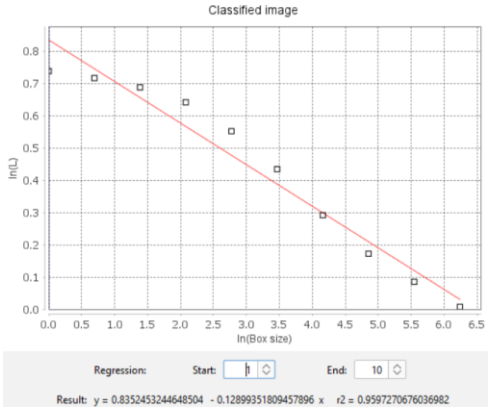

Fig. 11. Logarithmic Plot of Calculated Lacunarity Values Against Increasing Box Size

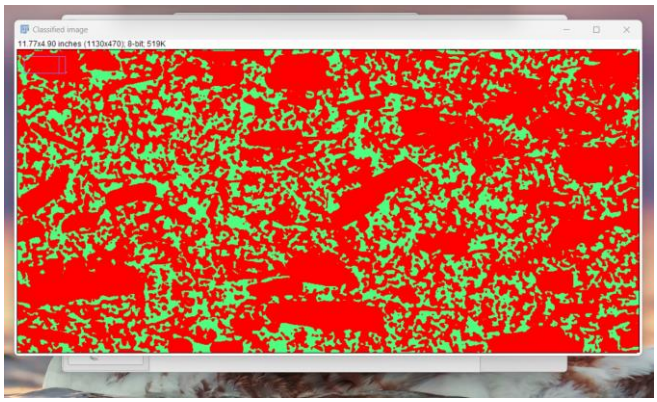

Fig. 12. Classified Output Image from TWS Showing Microstructural Appearance of the Sintered Ag Bond Line

In Equation 1, $E(x)$ represents the expected value of x while $M(r) = A(r)r^D$ denotes the contained within a box of size r constrained by the condition $\log A / \log r \to 0$ [5]. In Equation 2, BS refers to the box size in pixels, n indicates the total number of box divisions over an image, OP is the occupation percentage, PR represents the applied pressure of the percolating fluid, and pc corresponds to the position on x or y of the centroid of the box on the scale of pressure [6].